Axial performance of steel splice connection for tubular FRP column members

Chengyu Qiu[a], Chenting Ding[a], Xuhui He[b,*], Lei Zhang[b], Yu Bai[a,*]

[a] *Department of Civil Engineering, Monash University, Clayton, VIC 3800, Australia*
[b] *School of Civil Engineering, Central South University, Changsha, China*

ARTICLE INFO

ABSTRACT

A splice connection is proposed for connecting tubular fibre reinforced polymer (FRP) members. This connection consists of a steel bolted flange joint (BFJ) and two steel-FRP bonded sleeve joints (BSJs). The BFJ connects two steel hollow sections, each of which is telescoped into the targeted tubular FRP member through adhesive bond, forming a BSJ. To evaluate the performance of the proposed splice connection under axial loadings, BSJs of four different bond lengths and BFJs of two bolt configurations are tested individually. Finite element (FE) models are developed which feature a bilinear bond-slip relation, contact behaviours and bolt pre-tensioning. Comparisons are made between experimental and FE results in terms of load-displacement behaviours, ultimate capacities and strain responses. Besides being capable of identifying an effective bond length for the BSJ and modelling the yielding process of the BFJ, FE analysis provides insight into the distribution of adhesive shear stress over the bond area of the BSJs, and the steel yield line pattern on the flange-plate of the BFJs. Verified by experimental results, the FE modelling technique is then utilised to understand the integrated axial behaviours of a complete splice connection.

1. Introduction

Fibre reinforced polymer (FRP) composites are increasingly used in civil engineering structures, thanks to their high specific strength, superior corrosion resistance and availability in various geometries [1–3]. In particular, glass FRP (GFRP) composites are credited with sufficient strength and stiffness at moderate cost. Advances in the pultrusion manufacturing technique [4,5] have enabled mass production of GFRP profiles at reduced cost with satisfactory quality control, motivating research into their application as bridge decks [6,7], reinforcement [8], roof structure [9], trusses [10–12] and floor systems [13–15]. Compared to open section profiles (i.e. I or channel profiles), closed section profiles (i.e. circular or rectangular tubular profiles) exhibit better resistance against torsional and global buckling [16]. Yet these merits of tubular GFRP members coexist with the difficulty of connecting the members into truss and frame assemblies, due to the material anisotropy and the closed section shape.

Extensive research has been conducted in pursuit of viable connection forms for tubular GFRP members. Imitating practices in steel structures, early efforts to connect GFRP tubular members utilised bolted-through web-gusset plates or flange-angle cleats for beam-column connections [17]. In the development of a connection form for

axially loaded tubular GFRP profiles, the benefits of using a steel tubular sleeve connector which was inserted into and bolt-fastened to the tubular GFRP profile were underlined in [18,19]. This steel sleeve connector facilitated versatile connection forms to adjacent members. Despite the convenience of in-situ installation, bolt fastening requires hole-drilling on the composite material, creating problems such as damaged fibre architecture, stress concentration, and exposure of the weak in-plane shear strength of the FRP composites. Adhesive bonding, as an alternative, offers structural integrity, reduced stress concentration and also improved fatigue resistance [20–22]. Combining the benefits of the adhesive bond and the steel sleeve connector, bonded sleeve connections for joining circular GFRP truss members to nodal joints were proposed and examined in [11,12]. In an experimental investigation by Wu et al. [23] and the accompanying numerical study [24], the FRP-steel tubular bonded sleeve connection concept was utilised in FRP beam to steel column configurations. Such connections exhibited significant improvement in both rotational strength and stiffness over steel angle connections and bolted sleeve connections.

Despite the aforementioned works, research into developing a column-splice connection for FRP tubular members remains scarce. In steel structures, a widely used splice connection for rectangular/square hollow sections (RHS/SHS) is the bolted flange joint (BFJ), which
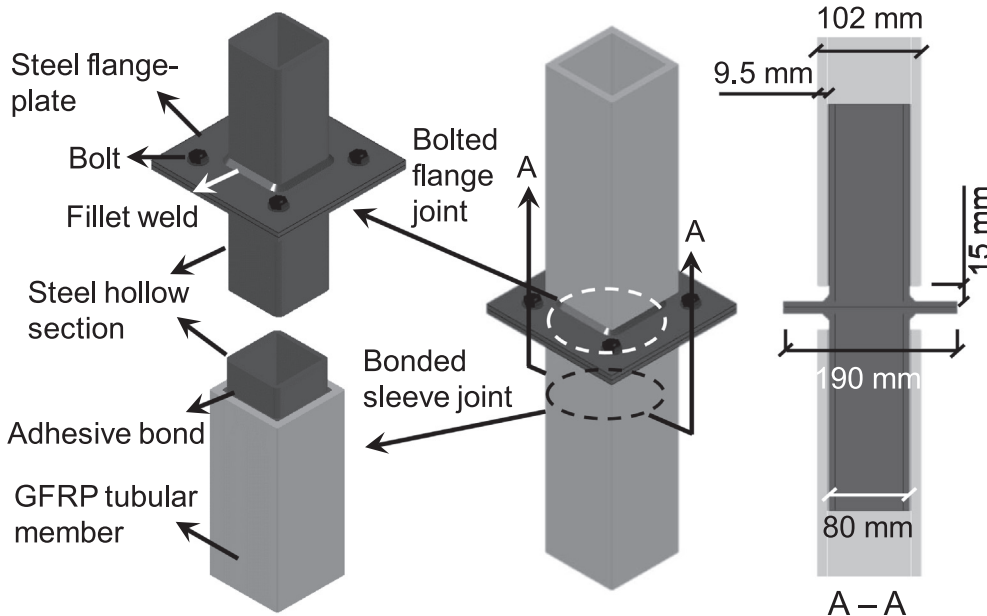
possesses the benefits of simple constitution and convenient in-situ installation [25]. Combining the FRP-steel bonded sleeve joint and the steel hollow section bolted flange joint, a column-splice connection for GFRP tubular members is proposed as illustrated in Fig. 1. This steel-GFRP connection system consists of two components: a bonded sleeve joint (BSJ) coupling GFRP and steel tubes adhesively, and a bolted flange joint (BFJ) connecting two steel SHSs through fillet weld. The BSJ reduces stress concentration in the GFRP compared to bolt fastening, while the BFJ enables convenient installation and imparts ductility to the system (through steel yielding). As presented in Fig. 1, for a pultruded FRP box section of $102 \times 102 \times 9.5$ mm, a steel SHS of outer dimension of 80×80 mm is selected in this study to achieve an adhesive thickness of 1.5 mm for practical assembly. To accommodate the fillet weld and to remove rotational constraint, a gap of 15 mm exists between the GFRP tubular member and the steel flange-plate. Steel flange-plate of 190×190 mm is selected for practical installation of the fastener (M12 bolt) and to fulfil the requirements for the edge distances of the fastener according to AS4100 [26]. Different loading scenarios may be found for the proposed splice connection depending on its potential applications. When used as a column splice, the connection is mainly subjected to a combination of axial (as a combination of tension and compression) and flexural loadings. When used as a beam splice, it would be under flexural and shear loadings. This paper focuses on investigating the performance of the proposed connection under axial loadings for column application.

Axial loading on the BSJ is resisted by shear between the GFRP and the steel adherends. Such a load transfer mechanism has been extensively studied in the form of single or double lap joints. A bilinear relationship has been widely utilised to model the bond-slip behaviour due to its simple constitution and hence convenient analytical and numerical implementation. This bilinear relationship is characterised by a linearly ascending stage between the adhesive shear stress and relative slip between the adherends, followed by a linear decrease to zero shear stress at the debonding slip.

Early analytical study took advantage of this relationship to solve for the axial capacities of single lap joints in several configurations [27,28] and also to identify the shear stress distribution [29,30] and debonding process [31]. Experiments were carried out to measure the shear stress-slip relationship along the bond line in FRP-concrete [32,33] and FRP-steel bonded lap joints [34–36], verifying that the bond-slip curves resembled a bilinear shape when brittle adhesives

were used. For ductile adhesives, meanwhile, a trapezoidal shape was found suitable [36,37]. The bilinear bond-slip relationship was incorporated into numerical analyses through the technique of cohesive zone modelling [38–40], in which a crack interface was pre-defined for the bond area and the tangential traction-slip relationship was defined as the bilinear shape. In light of previous work on single and double lap joints, an analytical solution, verified by experiments and FE analysis, was recently developed for the joint capacity of bonded sleeve connections consisting of circular steel and FRP tubular members [41]. In contrast to the earlier studies where adhesive shear stress was uniform in the transverse direction of single/double lap joints or in the circumferential direction of a circular section, the proposed connection, involving square or rectangular tubular adherends (Fig. 1), is distinguished by varying shear stress distribution in the transverse direction.

The failure mechanism of the bolted flange joint (BFJ) in axial loading of tension (more critical than in compression) is governed by a yield line mechanism in the steel flange-plate or/and tensile failure of the bolts under prying action. Taking into account both types of failure, design models were developed in [42] for configurations where one or two bolts were positioned at each side of the SHS. A similar design approach was later employed to solve for the layout with bolts at two sides of the RHS [43]. Focusing on the bolt failure under tensile loading, well-instrumented experiments were conducted to investigate the prying action on the bolts [44], before a modified AISC design procedure [45] was formulated. Design method is provided in Section 6 of Eurocode 3 Part 1–8 [46] to calculate the moment resistance of bolted flange splices or beam-column connections. Three modes of local yield lines are considered around the bolt holes at the tensile flange. Although this method is intended for I or H sections under bending loading, adaptation can be made as suggested in [47] and by mirroring the yielding lines at the tensile flange to calculate the tensile resistance of RHS/SHS bolted flange joints with bolts at two sides of the hollow section. The aforementioned experimental and analytical studies centred on the ultimate load-carrying capacities, and very limited description was presented of stiffness, failure processes and strain responses. Finite element (FE) methods were successfully utilised to understand the bending behaviour of these BFJ with [48] and without stiffeners [49]. Yet modelling results for the tensile behaviour of BFJs are still limited.

The remainder of this paper experimentally and numerically

investigates the mechanical performance of the proposed column-splice connection in axial loadings. Design parameters for the specimens include four different bond lengths and two types of bolt configuration (four and eight bolts). The detailed three-dimensional FE models feature utilising the bilinear bond-slip relationship for bond behaviour, contact between assembled parts and bolt pre-tensioning. Experimental results are then discussed and compared with FE modelling with respect to load-displacement behaviours, strain data, effect of bond length and yield line patterns of the connections. Finally, design recommendations are provided for optimising the performance of the proposed column-splice connection.

2. Experimental program

2.1. Specimens

As the proposed connection consisted of bonded sleeve joints (BSJs) and bolted flange joint (BFJ) in series as described in Fig. 1, experiments were conducted individually on each component. Considering shear failure within the adhesive layer (cohesive failure) as the failure mode of interest for the BSJs, tensile and compressive loadings would theoretically induce identical adhesive shear stress distribution along the bond length and thus identical joint behaviour [41]; therefore, only compression tests were conducted on the BSJ specimens. For the BFJs, compressive failure would be preceded by member failure of the connected steel hollow section member, for which reason only the tensile behaviours of the BFJs were investigated.

Each of the BSJ specimens, illustrated in Fig. 2, was fabricated from a pultruded GFRP square tube (102 × 102 × 9.5 mm), a grade 355 steel square hollow section (SHS, 80 × 80 × 6 mm) and Sikadur-30, a two-component epoxy-based structural adhesive. The BSJs were coded '*BSJ-x-y*' where '*x*' represents the bond length in mm (*x = 50, 100, 140 or 180*) and '*y*' refers to the index of the repeating specimen in each bond length (*y = 1 or 2*). Bonded surfaces of the steel and GFRP were pretreated by a procedure of 'degreasing – sandblasting – acetone cleaning' before adhesive was applied, as recommended in [50]. Fabrication of the specimens was followed by a 2-week curing under room temperature before testing.

Two types of bolt configuration were adopted for the BFJs, with their geometries shown in Fig. 3. These two configurations were doubly symmetric and were efficient in resisting both tensile and bending actions. The BFJs were coded '*BFJ-a-b*' where '*a*' represents the bolt number (*a = 4 or 8*) and '*b*' the index of the repeating specimen (*b = 1*

or *2*). BFJ-4 and BFJ-8 specimens shared the same geometries except for the number of bolts and their positions. Fillet welds of approximately 6 mm joined the steel SHS (80 × 80 × 6 mm, same as those in the BSJs) to the 6 mm-thick grade 250 steel flange-plate as shown in Fig. 3. During the welding, the flange-plate was clamped firmly against a rigid flat base to prevent likely deformation caused by heat distortion. A gusset plate was slot-welded into each steel SHS to enable application of tensile loading through gripping (Fig. 3a). The bolts were M12 grade 8.8 hex bolts with washers and nuts, pre-tensioned to around 52 kN (70% of the nominal proof load of the bolt) by a torque wrench before testing according to [45].

2.2. Material properties

The pultruded GFRP square tubes were composed of a polyester matrix (volume fraction 53.3%) and E-glass fibres (volume fraction 46.7%) [51]. The strength and elastic modulus properties of the GFRP material were determined in [51,52] according to relevant standard methods [53–55] as summarised in Table 1. The material properties of the steel SHS and flange-plate, tested from tensile coupons in accordance with ASTM A370-16 [56], are summarised in Table 2. The M12 bolt was reported to have a yield strength of 1043 MPa and Young's modulus of 235 GPa [24]. The Sikadur-30 adhesive, tested in [36] in accordance with ASTM D638-10 [57], exhibited linear brittle behaviour with tensile strength of 22.3 MPa and elastic modulus of 11.3 GPa.

2.3. Instrumentation and experimental setup

Compressive loading on the BSJ specimens was implemented by a 500 kN Amsler machine under displacement control at 0.4 mm/min loading rate (Fig. 4a). Axial shortening of the specimens was measured by two linear variable differential transducers (LVDT). As shown in Fig. 2a, strain gauges were installed on the surface of the GFRPs along the centre bond line at 30 mm intervals; two additional strain gauges were installed on the BSJ-180s offset 25 mm from the centre bond line, as indicated. The BSJs were each loaded past their peak load.

Tensile loading on the BFJ specimens was carried out by a 500 kN Baldwin machine at a 0.5 mm/min loading rate (Fig. 4b). A laser extensometer was used to gauge axial elongation of the specimens. Besides strain gauges G1 and G2 on the steel SHS (Fig. 3a), strain gauges G3 to G5 were installed on the flange-plate where, from trial FE analysis, yield lines were likely to form (Fig. 3b). The BFJs were each loaded until substantial yielding deformation of the steel was observed in the load-displacement curve.

3. Finite element modelling

3.1. Geometric modelling and material definitions

FE modelling of the specimens under axial loadings was performed using the commercial software ANSYS. Fig. 5 shows representative meshed models of the BSJ and BFJ specimens, for each of which half of the geometry was constructed due to symmetry. All the GFRP and steel components were meshed with SOLID185, a 3-D 8-node element in ANSYS. The GFRP was modelled as an orthotropic linear elastic material whose longitudinal direction aligned with the X-axis shown in Fig. 5a. The walls of the tubular GFRP members were idealised as transversely isotropic composite laminates, resulting in identical interlaminar and in-plane shear modulus (Table 1). The longitudinal and transverse elastic modulus of the GFRP were defined according to the values in Table 1. The steel SHS and flange-plate were modelled as isotropic multilinear work-hardening materials, representing the stress-strain curves measured from the tensile coupon tests. The fillet welds were considered to be the same material as the steel flange-plate.
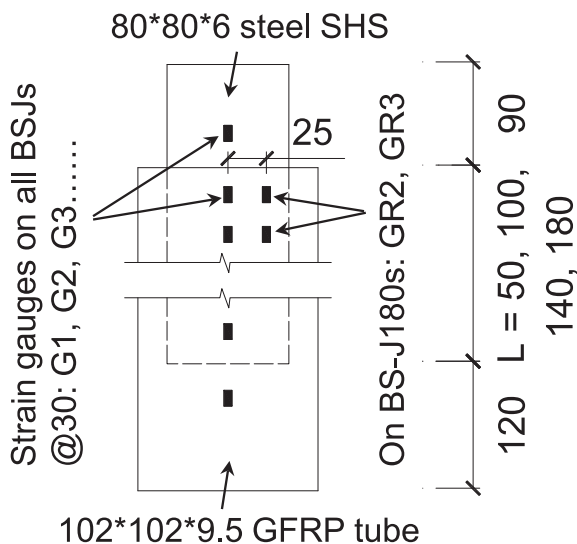

Fig. 2. Geometries of bonded sleeve joint specimens BSJ-50 to 180 and positions of strain gauges (all units in mm).
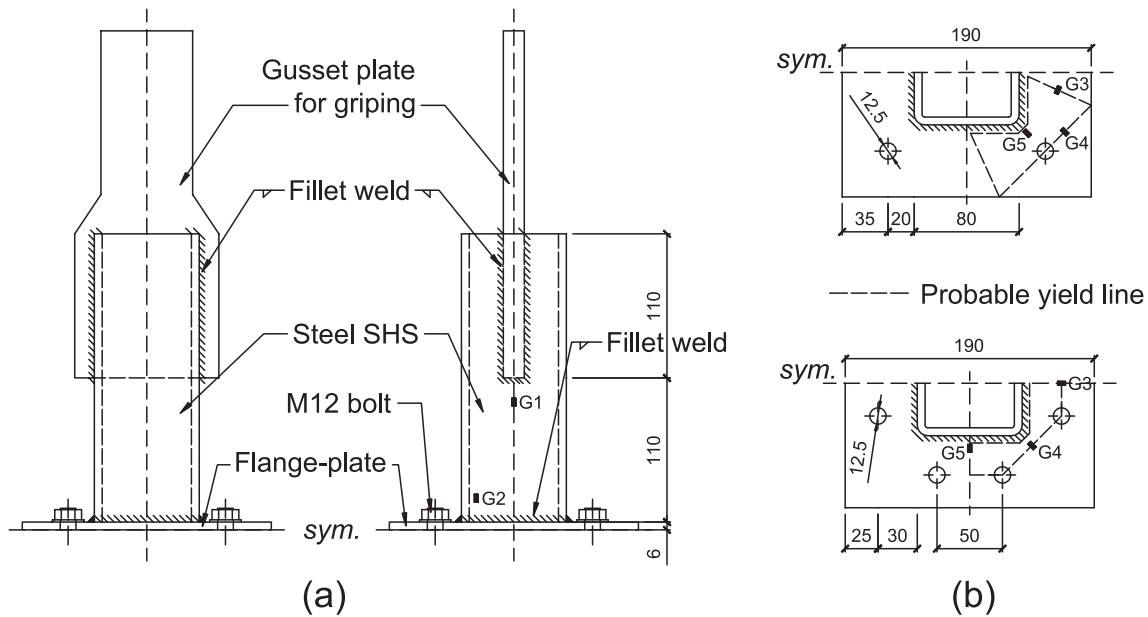
Fig. 3. (a) Front and side view of a BFJ-4 specimen; (b) plan views of BFJ-4 and BSJ-8 and positions of strain gauges (all units in mm).

Table 1
Strength and stiffness of the GFRP material.

Orientation and component	Strength (MPa)	Stiffness (GPa)	Method
Longitudinal tensile	306.5 ± 18.0	30.2 ± 1.4	ASTM D3039 [53]
Transverse tensile	–	5.5 ± 0.7	ASTM D3039 [53]
Interlaminar shear	26.7 ± 0.2	–	ASTM D2344 [54]
In-plane shear	14.9 ± 1.3	3.5 ± 0.7	10° off-axis tensile test [55]

Table 2
Strength and stiffness of the steel materials.

Steel component	Yield strength (MPa)	Ultimate strength (MPa)	Young's modulus (GPa)	Poisson's ratio
80 * 80 * 6 mm SHS[a]	420.1 ± 5.9[b]	519.4 ± 8.4	209.5 ± 3.9	0.277 ± 0.07
6 mm-thick flange	313.6 ± 1.0	458.5 ± 0.0	200.6 ± 2.2	0.277 ± 0.01

[a] Tensile coupons cut from walls of the tube.
[b] 0.2% offset yield strength.

3.2. Modelling bond behaviour in BSJs

Bond behaviour in the FE analysis was established through the cohesive zone modelling (CZM)) approach. This was enforced by a contact pair on the bonded surfaces, i.e. CONTA174 and TARGE170, a pair of 3-D 8-node surface-to-surface contact elements, applied on the bonded surface of the GFRP and steel respectively (Fig. 5a). A 1.5 mm-gap existed between the contact surfaces, representing the thickness of the adhesive layer. The normal stiffness of the contact interaction (both opening and closing) was input as the product of the elastic modulus and the thickness of the adhesive. The tangential traction between the contact surfaces was modelled as a bilinear function of the shear slip between the contact pair, as shown in Fig. 6. This bilinear bond-slip relationship, consisting of a linear ascending elastic stage, a linear descending softening stage and also a debonding stage with zero shear stress, has been deemed appropriate for modelling cohesive failures in bonded lap joints when brittle adhesives are used [34–36]. It should be

noted that, in the CZM approach, the distribution of shear stress was considered uniform through the thickness of the adhesive layer.

To define this bilinear relationship in ANSYS, three material parameters were required – the peak shear stress (τ_f), the stiffness of the elastic stage ($K_a = \tau_f/\delta_1$) and the critical fracture energy ($G_f = \tau_f \delta_f/2$). For the same adhesive (Sikadur-30) with identical layer thickness ($t_a = 1.5\,mm$), the peak shear stress ($\tau_f = 18.4\,MPa$) and critical fracture energy ($G_f = 1.25\,N/mm$) had been determined in a previous experimental investigation of steel-FRP single lap joints [36]. Assuming uniform shear stress thus shear strain through the thickness of the adhesive layer, the stiffness K_a was calculated by:

$$K_a = G_a t_a \tag{1}$$

where G_a is the adhesive shear modulus calculated from the elastic modulus with a Poisson's ratio of 0.3, and t_a is the thickness of the adhesive layer.

Before applying the axial loading, the GFRP end was constrained in all directions and symmetric constraint was applied on the longitudinal cut plane (XZ plane in Fig. 5a). A load step which displaced the steel end in tension or compression was solved with automatic time-stepping for better convergence. It was further confirmed that tensile and compressive loadings generated identical load-displacement behaviour and shear stress distribution between the bonded surfaces.

3.3. Modelling contact and pretension in BFJs

In the modelling of the BFJs, contact between the assembled steel components was considered by the contact pair CONTA174 and TARGE170, with a steel-to-steel friction coefficient of 0.44 [58]. Three contact pairs were identified as shown in Fig. 5b, i.e. those between the two flange-plates, between the bolt washer and flange-plate, and between the bolt shank and hole. Bolt pretension was applied via PRETS179 elements defined at the midsection of each bolt shank (Fig. 5b). In terms of boundary conditions, one end of the specimen was constrained in all directions and symmetry constraint was applied on the longitudinal cut plane (XZ plane in Fig. 5b). Application of the bolt pretension was solved in a first load step before a second load step axially displaced the free end of the specimen in the tensile direction.
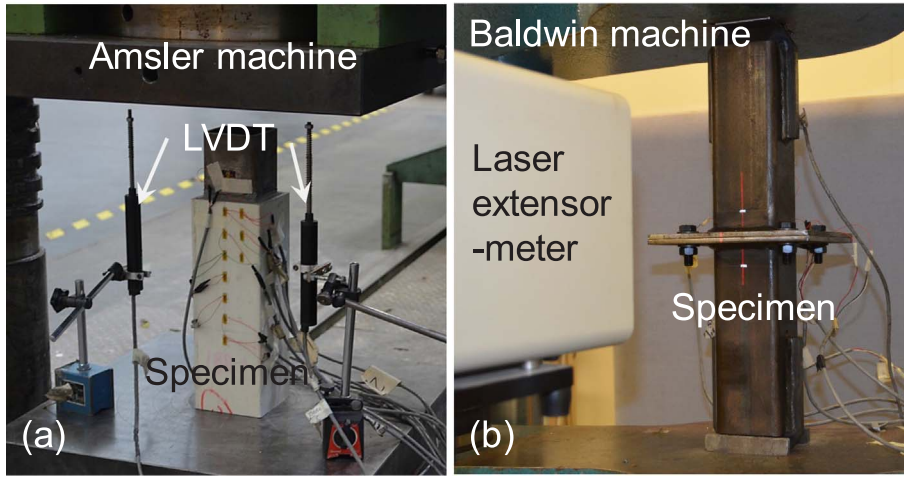
4. Results and discussion: BSJ specimens

4.1. Failure modes and load-displacement responses

Experiments revealed brittle cohesive failure within the adhesive layer of all the BSJs. Fig. 7 shows typical load-displacement curves of the BSJs, characterised by a linear increase to peak load before brittle failure. Post-failure residual strength, provided by friction on the fracture surfaces, was recorded between 10 and 45 kN among specimens. Likewise, as also shown in Fig. 7 linear brittle load-displacement behaviours were produced by FE modelling, except that the experimental residual strength could not be captured. Of all the BSJ specimens, discrepancy in the stiffness is found no more than 18% between experiment and FE modelling. When the peak load was imminent, cracking in the adhesive layer was observed as shown in Fig. 8a. In BSJ-100-1 and BSJ-140-1, post-failure loading resulted in cracks at the web-flange junction of the GFRPs, as indicated in Fig. 8b, possibly due to the confining pressure generated through sliding of the adherends over the uneven crack surface. Fig. 8c, representative of all BSJs, shows the separated adherends and the crack surface where bond failure occurred; the attachment of adhesive to both the steel and GFRP indicates cohesive failure located within the adhesive layer but closer to the GFRP.

4.2. Joint capacity versus bond length

Table 3 summarises the experimental joint capacities ($P_{u,E}$) of all BSJs and the corresponding FE estimates ($P_{u,FE}$). Except for the BSJ-50
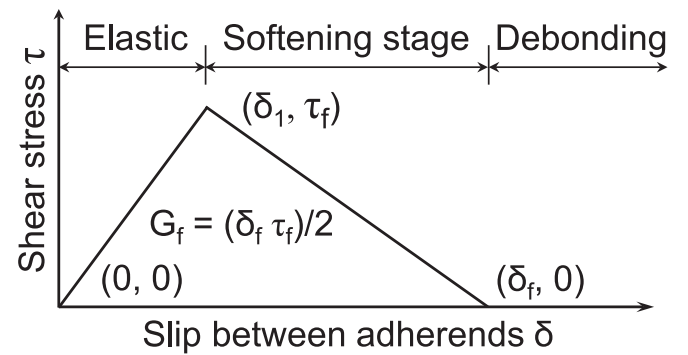

Fig. 6. Bilinear bond-slip relationship for GFRP-steel bond.

specimens (where $P_{u,E}/P_{u,FE} = 0.761$), the FE modelling compared well to the experimental results with differences less than 13%. For all BSJs, the overestimation by FE modelling may be due to the fact that the bilinear bond-slip relationship adopted in the FE analysis was derived from a plate-to-block single lap joint configuration [36], while the square tubular geometry of the BSJs imposed higher levels of through-thickness stress within the adhesive layer. This complex stress state in the adhesive, although dominated by shear stress, may advance expected bond failure. To account for the existence of the through-thickness stress in addition to the shear stress in the adhesive layer, application of a mixed-mode (mode I and mode II) bilinear bond
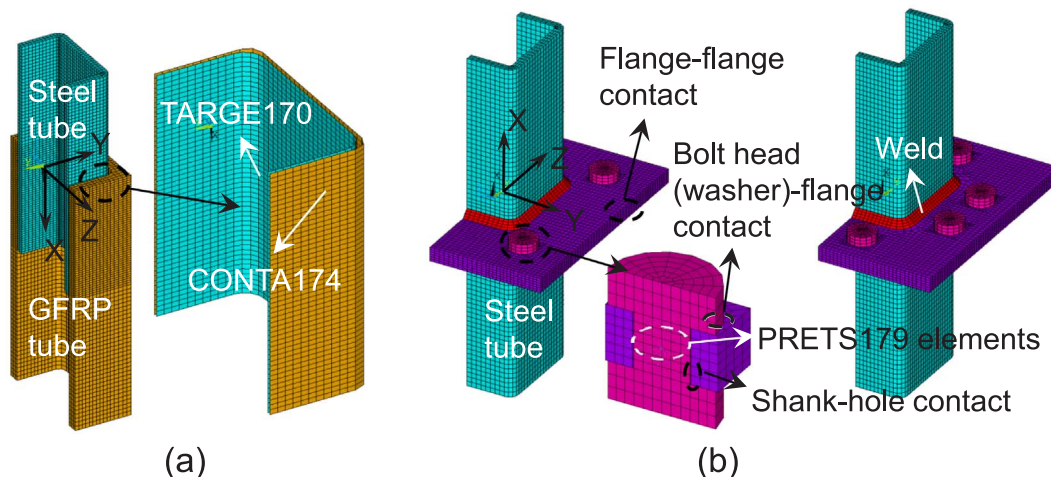

Fig. 5. Meshed FE models: (a) BSJ specimens; (b) BFJ-4 and BFJ-8 specimens.
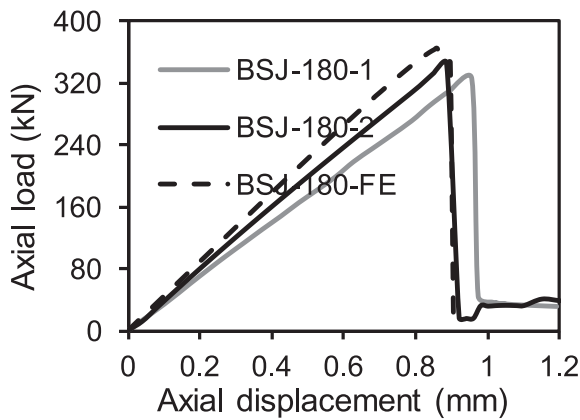
Fig. 7. Typical experimental and FE load-displacement curves of BSJs.

Table 3
Comparison of experimental and FE joint capacity of BSJs.

Bond length L (mm)	Experimental joint capacity $P_{u,E}$ (kN)			FE joint capacity $P_{u,FE}$ (kN)	Accuracy ($P_{u,E}/P_{u,FE}$)
	1	2	Average		
50	155	166	160.5 (± 3.4%)	211	0.761
100	303	266	284.5 (± 6.5%)	323	0.881
140	327	278	302.5 (± 8.1%)	346	0.875
180	326	346	336.0 (± 3.0%)	350	0.960

Fig. 9. Experimental and FE results of axial joint capacity versus bond length.

behaviour in the numerical modelling [59] may represent the experiment scenario more accurately. However, this requires determination of the cohesive parameters of both mode I and mode II [60]; while further experimental calibration is needed to acquire the mode I parameters for this study. It should also be noted that implementation of the mixed-mode model in the contact behaviour often encounters with convergence difficulty for the 3-D modelling as in this study although such mixed-mode bond behaviour was successfully applied in 2-D FE modelling [59]. The overestimation of joint capacities can also be attributed to the thicker adhesive layer at the corners (due to the round corners of the steel SHS) where local bond strength may be compromised. Joint capacities $P_{u,E}$ and $P_{u,FE}$ versus bond length (L) are plotted in Fig. 9. The increase in $P_{u,E}$ with L slowed dramatically after around $L = 100\,mm$, which was successfully captured by the FE modelling, indicating an effective bond length of 100 mm.

4.3. Strain responses

The specimen BSJ-180-2 sustained the greatest axial load of all the BSJs. Its load-strain responses recorded by strain gauges outside the bond region (G1 and G8) are plotted in Fig. 10. The linear responses and the strain values indicated that both the steel and the GFRP adherends were within elastic range. From the same specimen, axial strains on the outer surface of the GFRP along the centre bond line, at four different load levels from FE modelling as well as experiment, are plotted in Fig. 11. It is evident that the axial strain distribution at mid-portion of the bond length features a flatter gradient, revealing lower levels of shear stress in this region than at the ends of the bond length. In general, the axial strain distribution near the GFRP end of the bond length ($x = 180\,mm$) exhibits a steeper gradient than at the steel end ($x = 0\,mm$), matching anticipation that greater shear slip (δ) would occur near the more flexible adherend (GFRP in this case). Also noteworthy is that in Fig. 11d (corresponding to 100% P_u) the strain distribution flattens near the GFRP end, indicating a drop of adhesive
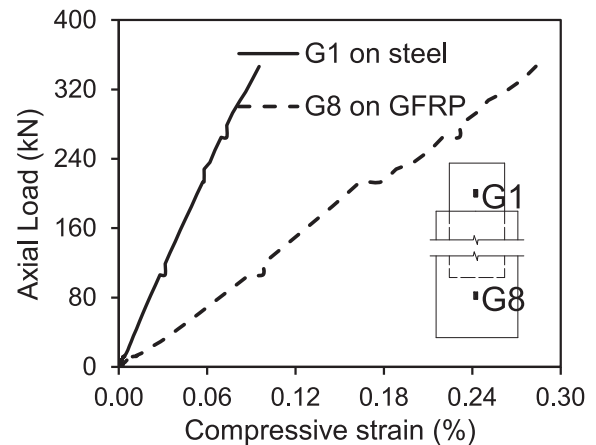

Fig. 10. Load-strain behaviour from strain gauges installed outside bond area (BSJ-180-2).

shear stress as a result of the GFRP end being loaded into the softening stage (see Fig. 6). The discrepancy between the experimental and FE strain data derives from two main sources. One is approximation of the true bond-slip relationship into a bilinear shape; the other source is that
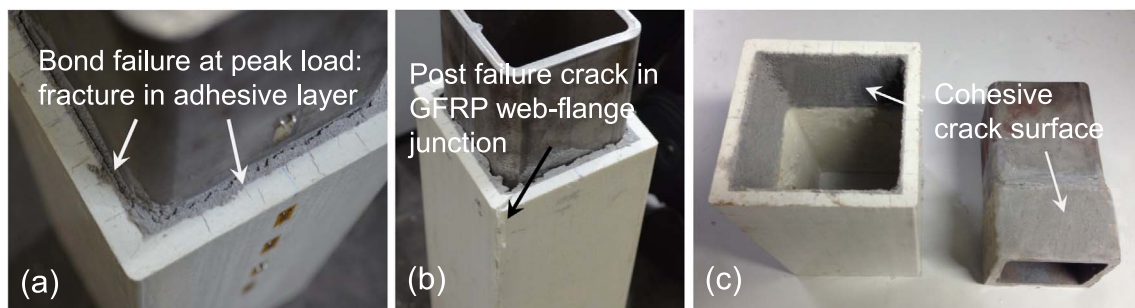

Fig. 8. Failure modes of BSJs: (a) adhesive failure at peak load; (b) cracking of GFRP after peak load (BSJ-100-1 and BSJ-140-1); (c) bond failure surface.
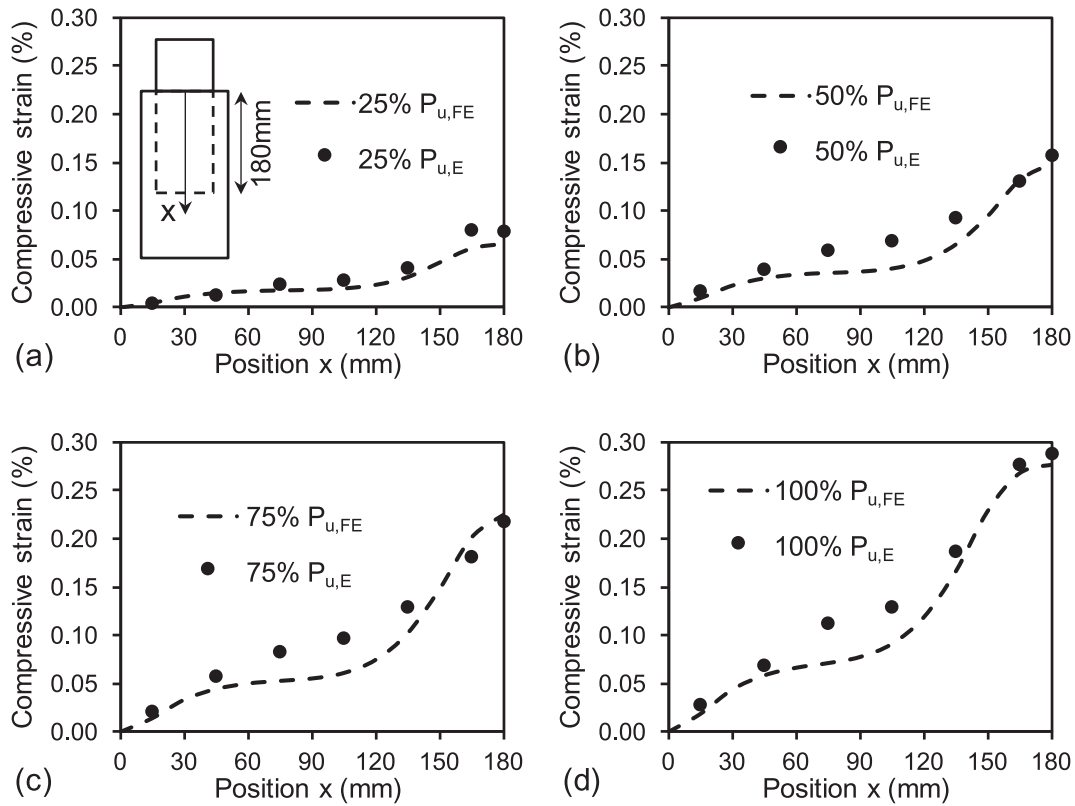
Fig. 11. Experimental and FE results of axial strains on the outer surface of the GFRP along centre bond line (BSJ-180-2, positions of strain gauges indicated in Fig. 2) at (a) 25% P_u; (b) 50% P_u; (c) 75% P_u; (d) 100% P_u.

the GFRP was approximated as uniform through its wall thickness, instead of its actual mat-roving-mat layered structure.

4.4. Adhesive shear stress distribution

Fig. 12 shows, from FE analysis, the distribution of adhesive shear stress along the centre bond line at four different load levels of BSJ-180 as a representation for all the BSJs. At 25% and 50% P_u, the full bond length is within the elastic stage of the bilinear bond-slip curve (Fig. 6); the majority of the shear resistance is provided near the two ends of the bond line and the maximum shear stress (τ_f) appears at the GFRP end ($x = 180$ mm, as the more flexible adherend). The increase of load from 50% to 75% P_u introduces a drop in shear stress near the GFRP end, due to its moving past the peak shear stress point (δ_1, τ_f) in the bilinear curve before entering the softening stage. As P increases further to

Fig. 12. FE results of shear stress distribution along centre bond line at different load levels of BSJ-180.

100% P_u, the softening length at the GFRP side extends inwards while the rest of bond length remains in the elastic stage.

Fig. 13 presents, at peak loads, the FE results of shear stress distribution over the entire bond area for all the BSJs. In contrast to single/double lap joints or circular bonded sleeve joints, non-uniform adhesive shear stress in the BSJs is found in the transverse direction (z direction). Generally, higher shear slip (δ) is induced further from the centre bond line, due to the greater rigidity at the corners of the tubular adherends than in the flat wall regions. The gradient of the transverse variation is flatter near the two longitudinal ends ($x = 0$ mm and 180 mm) and steeper inwards. The transverse variation of shear stress is implicitly evidenced by the experimental load-strain curves (BSJ-180-1) shown in Fig. 14; consistent with the FE output, the GFRP axial strains closer to the transverse corner of the adherend (GR2 and GR3) are greater than those along the centre bond line (G2 and G3).

In consideration of the shear stress distribution at peak load (100% P_u), the bond areas of the four BSJs could each be divided into two regions: a softening zone as highlighted in Fig. 13 and the remaining elastic zone, the boundary between the regions being defined by a line of the peak shear stress τ_f. Fig. 13a presents a typical shear stress distribution at peak load with a short bond length (BSJ-50). Near the location where $z = 38$ mm (the adherend transverse corner), the full bond length is loaded into the softening stage of the bilinear curve. Fig. 13b–d share typical stress distributions for longer bond lengths (BSJ-100, 140, 180). Stress distribution along the x direction can generally be characterised by an elastic zone near the steel side and a softening zone near the GFRP side, with the debonding point of the bilinear curve (δ_f, 0) attained at the GFRP end close to the transverse corners of the steel SHS (i.e. $z = 38$ mm). In Fig. 13b, c, and d, as the bond length increases, the softening zone does not exhibit notable change whereas the low-stress region in the elastic zone expands markedly. This observation signifies an inefficient increase in bond strength, thus implying the existence of an effective bond length.
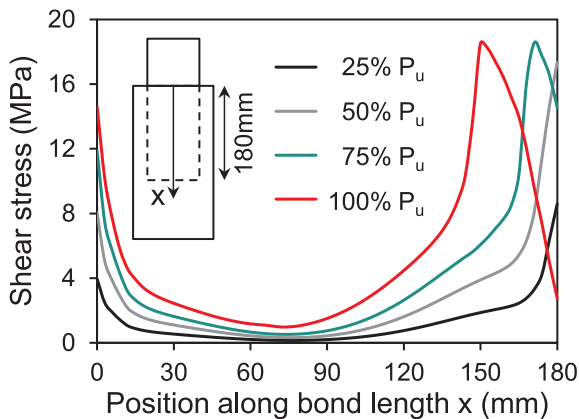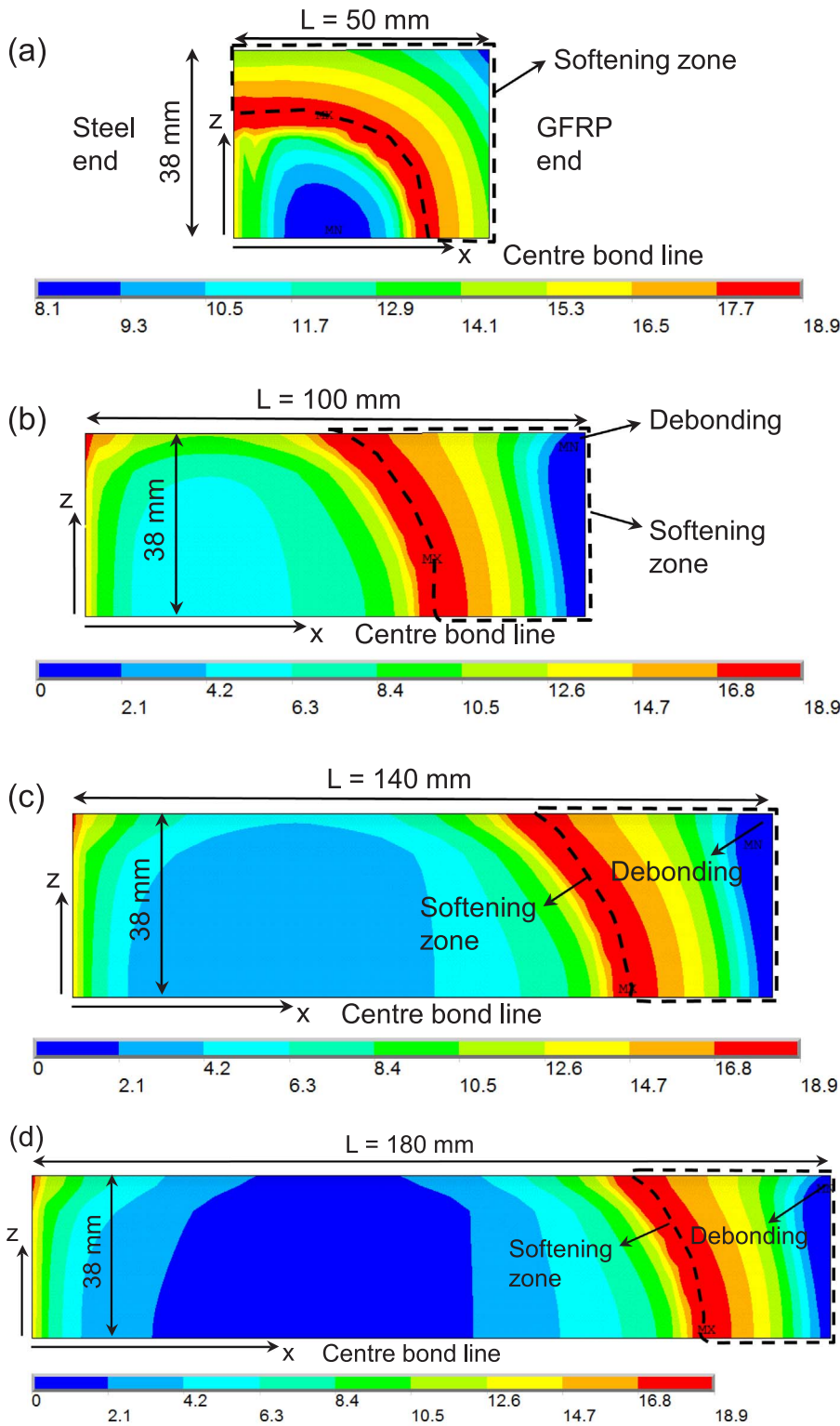
5. Results and discussion: BFJ specimens

5.1. Failure modes and load-displacement behaviours

All the BFJ specimens failed through steel yielding with notable deformation of the flange-plates; no bolt deformation was visible but the nuts were found to loosen after loading. As shown in Fig. 15, elongation of BFJ-4 (i.e. BFJ with four bolts) resulted in opening gaps between the two flange-plates in the region away from the bolts; while in BFJ-8, the flange-plates were bent outwards near the location welded with the SHS. Fig. 16 presents the tensile load-displacement behaviours of the BFJs. After steel yielding, the load-displacement curves kept increasing gradually at near constant slopes until the loading process was ceased at 9 mm elongation for the BFJ-4s or at 8 mm for the BFJ-8s.

The initial stiffness of the BFJs (S_i) is defined as the slope of the linear stage of the load-displacement curves, and yield capacity (P_y) is determined by the intersection of the elastic and post-yield tangent lines. Both experimental and FE values of S_i and P_y are summarised in
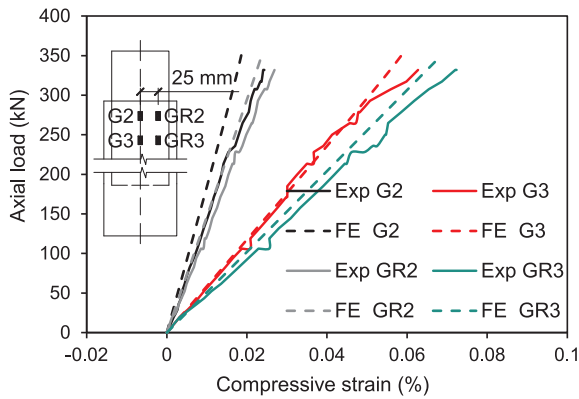
Fig. 14. Comparison of strain responses from 25 mm-offset and centre strain gauges (BSJ-180-1).

Table 4. From BFJ-4 to BFJ-8, an increase of four bolts improved the experimental stiffness ($S_{i,E}$) by 233% and the yield capacity ($P_{y,E}$) by 77%. Comparison between the FE and experimental results, presented in Fig. 15 and Fig. 16, shows that both the deformed shapes and the load-displacement behaviours were accurately captured by the FE modelling. As presented in Table 4, the FE results of stiffness ($S_{i,FE}$) are within 16% from experimental values, and the FE yield capacities ($P_{y,FE}$) within 8%. The slightly higher yield capacities obtained from the FE modelling may be a consequence of welding residual stress in the flange-plates of the experimental specimens.

5.2. Stress distribution and load-strain responses

Fig. 17 depicts from FE modelling the distributions of stress state ratio (defined as the ratio of von Mises stress to yield stress) for BFJ-4 at 114 kN and BFJ-8 at 198 kN, where a ratio larger than 1.0 indicates yielding of steel at the position. These stress distributions reveal that, as the loads increased beyond the yield capacities of the BFJs, the high stress areas formed into a pattern, allowing continuous yielding and thereby causing large elongation deformation of the specimens. Fig. 17 also presents the stress state of the bolts, indicating that the bolts were
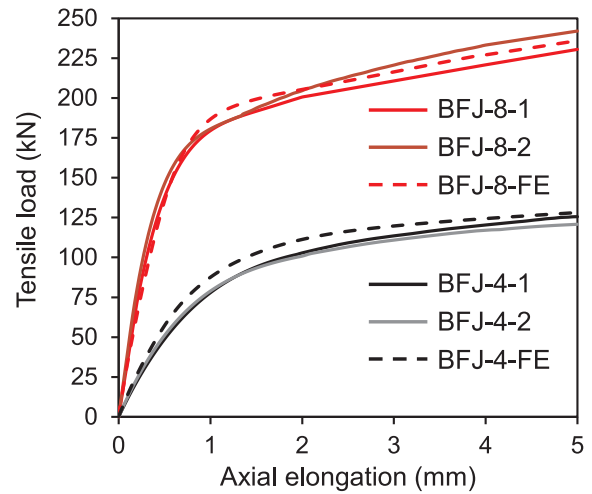

Fig. 16. Experimental and FE tensile load-displacement behaviours of (a) BFJ-4 and (b) BFJ-8.

Table 4
Comparison of yield capacity (P_y) and initial stiffness (S_i) of BFJs from experiment and FE modelling.

Specimen	$P_{y,E}$ (kN)[a,b]	$P_{y,FE}$ (kN)[b]	$P_{y,E}$ / $P_{y,FE}$	$S_{i,E}$ (kN/ mm)[a,c]	$S_{i,FE}$ (kN/ mm)[c]	$S_{i,E}/S_{i,FE}$
BFJ-4	104	113	0.920	104	117	0.889
BFJ-8	184	192	0.958	346	305	1.134

[a] Average value of the two repeating specimens.
[b] intersection point of the load-displacement curve's elastic and post-yield tangent lines.
[c] slope of the initial linear part of the load-displacement curve.

subjected to a combination of bending and tensile action, due to the prying effect from the deformed flange-plates. The bolts of BFJ-4 were found to be under greater stresses than those of BFJ-8, yet yielding was limited to less than 16% of the cross-section area of the bolt shank.

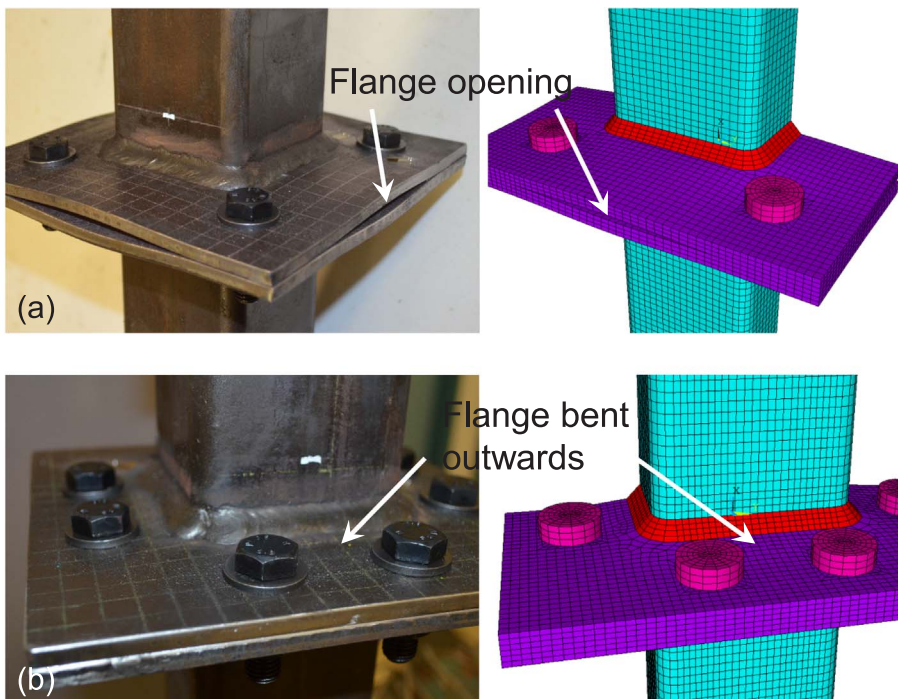Both experimental and FE load-strain curves are plotted in Fig. 18.

Fig. 15. Experimental and FE deformed shapes of BFJ specimens (a) BFJ-4 at 6 mm extension; (b) BFJ-8 at 5 mm extension.
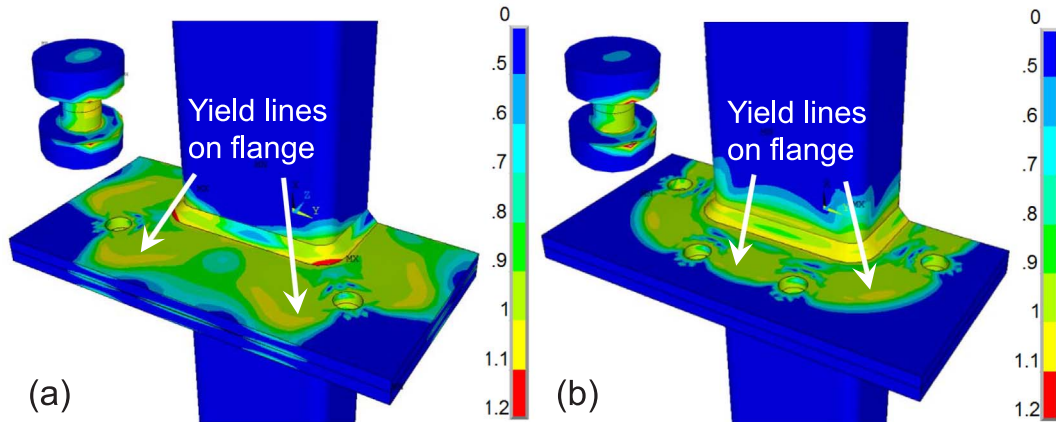
Fig. 17. Von-Mises stress state distribution (a) BFJ-4 at 114 kN; (b) BFJ-8 at 198 kN.

As the strain gauges G3 to G5 were installed at highly stressed locations and orientations, their readings can indicate the yield initiation of the specimens. For BFJ-4 (Fig. 18a), the experimental G3 curve deviates from initial linearity at around 50 kN tensile load, which resembles the beginning of nonlinearity in the load-displacement curve (Fig. 16a). Likewise for the BFJ-8, both the experimental G3 curve (Fig. 18b) and load-displacement curve (Fig. 16b) begin to exhibit nonlinearity at around 86 kN tensile load. The linear behaviour of G2 shown in Fig. 18b demonstrates that the SHS was within the elastic range for all the BFJs. Further, the experimental and FE load-strain curves show satisfactory agreement, especially when steel yielding has occurred.

6. Integrated performance of proposed splice connection

Given the bonded sleeve joint (BSJ) and bolted flange joint (BFJ) investigated in prior sections, the experiment-validated FE modelling approaches can aid understanding of the performance of the proposed splice connection as an integration of BSJ and BFJ under axial loadings. Fig. 19 presents the meshed FE model of a design example SC-180-8, namely a splice connection using 180 mm bond length and the BFJ-8 bolt configuration. The FE model of SC-180-8 incorporates all the features and details of BSJ-180 and BFJ-8 described in Section 3, i.e. geometries (with the 15 mm-gap distance between the GFRP tube and steel flange-plate as described in Fig. 1), element types, material properties and contact behaviours. The load-carrying performances of SC-180-8 in both tension and compression are also indicated in Fig. 19.

The tensile load-displacement behaviour of the design connection SC-180-8 is plotted as the black curve in Fig. 19. It is confirmed that the yielding and the subsequent hardening behaviour of SC-180-8 coincide with those of BFJ-8 (FE shown as the black dashed curve and

experimental as the black dotted curve), due to the same failure mode of flange-plate yielding. The initial stiffness of SC-180-8 differs from that of BFJ-8 due to the inclusion of the GFRP tube. With a gauged length of 640 mm used in Fig. 19, SC-180-8 exhibits slightly lower initial stiffness than BFJ-8. The ultimate load capacities of SC-180-8, both in tension and compression, are bounded by the axial joint capacity of BSJ-180, which is presented in Fig. 19 as the horizontal dashed line from FE modelling and the horizontal dotted line from the experimental result. Generally, for other bond lengths and bolt configurations used with the splice connection, the tensile performance may show either brittle or ductile responses. The former happens when axial capacity of the BSJ is attained before yielding of the BFJ; and the resulting load-displacement curve of the splice connection develops linearly before the brittle failure of the BSJ component. The latter takes place when yielding of the BFJ precedes failure of the BSJ as in the case of SC-180-8. In this case, the load-displacement curve flattens upon yielding of the BFJ component, and continues to develop at reduced stiffness until axial capacity of the BSJ is attained. Behaviour of the connection SC-180-8 under compression loading is presented as the solid grey line in Fig. 19. The compressive load-displacement curve ascends linearly until the axial capacity of BSJ-180 is reached, where the bond failure of the BSJ component occurs. Furthermore, design of the compressive performance of FRP tubular members with such a connection may also involve buckling of the FRP member or yielding of the steel SHS, depending on their geometries and material properties. The tensile behaviour of the designed splice connection, which is governed by that of BFJ-8, as discussed above, utilises yielding of the steel component, and therefore ductile performance before brittle bond failure is achieved.
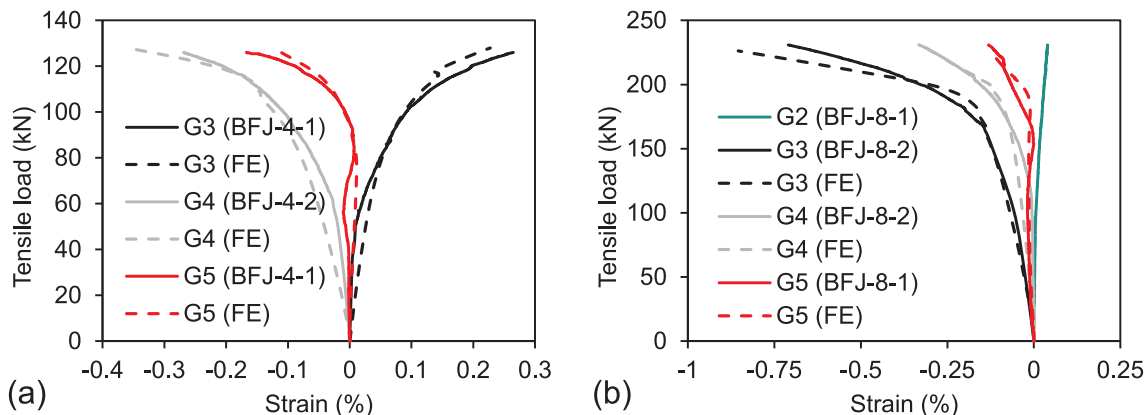

Fig. 18. Experimental and FE load-strain responses of (a) BFJ-4 and (b) BFJ-8 (refer to Fig. 2 for positions of strain gauges).
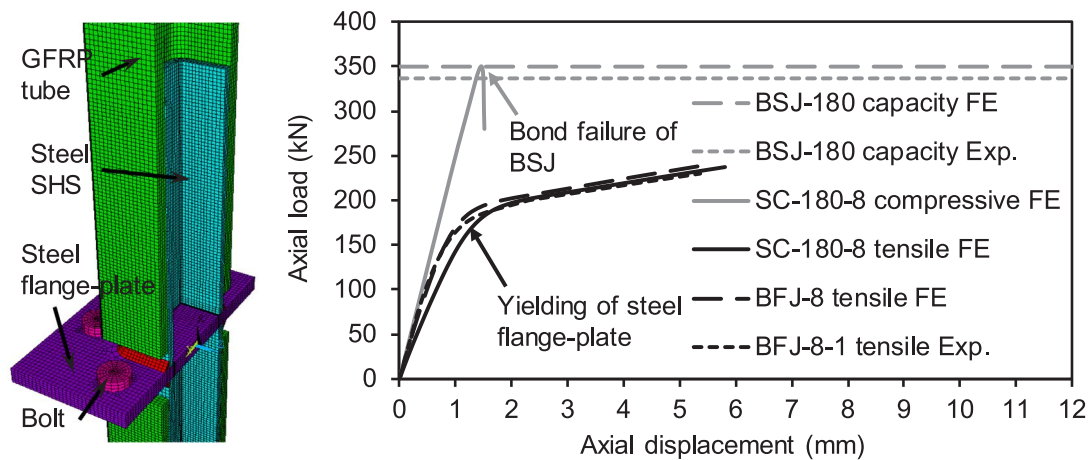
Fig. 19. Meshed FE model of a tubular FRP splice connection SC-180-8 and indication of its axial load-carrying performance.

7. Conclusions

A steel splice connection was developed to join tubular FRP members and its axial performance was investigated through experimental study and FE modelling. The two components of the splice connection, namely the bonded sleeve joint (BSJ) and bolted flange joint (BFJ), were first experimentally examined. FE modelling was performed to study and understand the failure modes, load-displacement behaviours and strain responses. Verified by experimental results, the FE modelling technique was applied to understand the axial performance of the proposed splice connection integrated by the BSJ and BFJ. From the present study, the following conclusions can be drawn:

1. Under axial loading, the BSJs failed in a brittle manner within the adhesive layer. Their load-displacement behaviour was linear up to peak load, followed by a sudden drop to residual strength between 10 and 45 kN. Among the four bond length groups (50, 100, 140 and 180 mm), FE analysis employing the bilinear bond-slip relationship produced estimates of joint capacity mostly within 15%. An effective bond length of around 100 mm was identified both experimentally and numerically for this joint configuration.
2. For the BSJ specimens, strain distribution on the GFRP surface indicated softening of the bond length at the GFRP end as the load increased and transverse variation of adhesive shear stress. The consistency between experimental and FE results for strain distribution further validated the FE modelling approach. Therefore the FE analysis provided insights into the adhesive shear stress distribution over the bond area. In the longitudinal direction, the GFRP (as the more flexible adherend) end of bond length sustained higher shear stress initially and, as the external load increased, entered the softening stage while the steel end remained elastic. In the transverse direction, a higher level of slip between the adherends occurred closer to the adherend transverse corner, resulting in earlier entry to the softening stage and ultimately longer softening length. At peak loads, two types of shear stress distribution were identified. For the BSJ specimen with 50 mm bond length (BSJ-50), the entire bond length near the adherend transverse corner was loaded into the softening stage. For other specimens with longer bond lengths (BSJ-100, 140 and 180), softening occurred near the GFRP side and the transverse corner of the GFRP end was loaded to the debonding point of the bilinear bond-slip relationship, while the rest of the bond area remained in the elastic stage.
3. Failure of the BFJs was ductile through yielding of the flange-plates. The load-displacement responses could all be characterised as a 'linear ascending – yielding – linear hardening' process. The eight-bolt configuration (BFJ-4), compared to the four-bolt one (BFJ-4),

improved the initial stiffness by 225% and the yield capacity by 82%. The FE modelling successfully captured the deformed shapes and produced load-displacement and load-strain responses that were in good comparison with experimental ones. The FE estimates of initial stiffness were within 14% of the experimental ones and those of yield capacity were within 8% of the experimental estimates. From review of the FE von Mises stress distributions on the flange-plates, the improvement in stiffness and yield capacity from BFJ-4 to BFJ-8 was revealed to be associated with a more optimal yield line mechanism which involved an enlarged yielding area.

4. The axial behaviours of a complete splice connection, integrating the BSJ and BFJ, could be studied through the experiment-validated FE modelling approach. A FE model of a splice connection, integrating the BSJ with 180 mm bond length and the BFJ with eight bolts (SC-180-8), was developed, with its load-carrying performance verified by experimental data. The tensile behaviour of SC-180-8, involving yielding of the BFJ below the ultimate load of the BSJ, demonstrated that ductile failure could be achieved by utilising the yielding of the steel component.

Acknowledgements

References

[1] Keller T. Recent all-composite and hybrid fibre-reinforced polymer bridges and buildings. Prog Struct Mat Eng 2001;3(2):132–40.
[2] Bakis C, Bank LC, Brown V, Cosenza E, Davalos J, Lesko J, et al. Fiber-reinforced polymer composites for construction-state-of-the-art review. J Compos Constr 2002;6(2):73–87.
[3] Hollaway L. A review of the present and future utilisation of FRP composites in the civil infrastructure with reference to their important in-service properties. Constr Build Mater 2010;24(12):2419–45.
[4] Bank LC. Composites for construction: structural design with FRP materials. John Wiley & Sons; 2006.
[5] Meyer R. Handbook of pultrusion technology. Springer Science & Business Media; 2012.
[6] Bank LC, Gentry TR, Nuss KH, Hurd SH, Lamanna AJ, Duich SJ, et al. Construction of a pultruded composite structure: case study. J Compos Constr 2000;4(3):112–9.
[7] Keller T. Use of fibre reinforced polymers in bridge construction. Zurich: International Association for Bridge and Structural Engineering (IABSE); 2003.
[8] Benmokrane B, El-Salakawy E, El-Gamal S, Goulet S. Construction and testing of an innovative concrete bridge deck totally reinforced with glass FRP bars: Val-Alain Bridge on Highway 20 East. J Bridge Eng 2007;12(5):632–45.
[9] Keller T, Haas C, Vallée T. Structural concept, design, and experimental verification

of a glass fiber-reinforced polymer sandwich roof structure. J Compos Constr 2008;12(4):454–68.

[10] Hagio H, Utsumi Y, Kimura K, Takahashi K, Itohiya G, Tazawa H. Development of space truss structure using glass fiber reinforced plastics. Proceedings of Advanced Materials for Construction of Bridges, Buildings, and Other Structures III, Davos, Switzerland. 2003.

[11] Bai Y, Zhang C. Capacity of nonlinear large deformation for trusses assembled by brittle FRP composites. Compos Struct 2012;94(11):3347–53.

[12] Yang X, Bai Y, Ding F. Structural performance of a large-scale space frame assembled using pultruded GFRP composites. Compos Struct 2015;133:986–96.

[13] Awad ZK, Aravinthan T, Zhuge Y. Experimental and numerical analysis of an innovative GFRP sandwich floor panel under point load. Eng Struct 2012;41:126–35.

[14] Satasivam S, Bai Y, Zhao X-L. Adhesively bonded modular GFRP web–flange sandwich for building floor construction. Compos Struct 2014;111:381–92.

[15] Satasivam S, Bai Y. Mechanical performance of bolted modular GFRP composite sandwich structures using standard and blind bolts. Compos Struct 2014;117:59–70.

[16] Wardenier J, Packer J, Zhao X, Van der Vegte G. Hollow sections in structural applications. Cidect Zoetermeer, Netherlands; 2010.

[17] Smith S, Parsons I, Hjelmstad K. Experimental comparisons of connections for GFRP pultruded frames. J Compos Constr 1999;3(1):20–6.

[18] Luo FJ, Bai Y, Yang X, Lu Y. Bolted sleeve joints for connecting pultruded frp tubular components. J Compos Constr 2016;20(1):04015024.

[19] Luo FJ, Yang X, Bai Y. Member capacity of pultruded GFRP tubular profile with bolted sleeve joints for assembly of latticed structures. J Compos Constr 2016;20(3):04015080.

[20] Kwakernaak A, Hofstede J. Adhesive bonding: providing improved fatigue resistance and damage tolerance at lower costs. SAMPE J 2008;44(5):6–15.

[21] Keller T, Gürtler H. Quasi-static and fatigue performance of a cellular FRP bridge deck adhesively bonded to steel girders. Compos Struct 2005;70(4):484–96.

[22] Zhang Y, Vassilopoulos AP, Keller T. Stiffness degradation and fatigue life prediction of adhesively-bonded joints for fiber-reinforced polymer composites. Int J Fatigue 2008;30(10):1813–20.

[23] Wu C, Zhang Z, Bai Y. Connections of tubular GFRP wall studs to steel beams for building construction. Compos B Eng 2016;95:64–75.

[24] Zhang Z, Wu C, Nie X, Bai Y, Zhu L. Bonded sleeve connections for joining tubular GFRP beam to steel member: numerical investigation with experimental validation. Compos Struct 2016;157:51–61.

[25] Kurobane Y. Design guide for structural hollow section column connections. Verlag TUV Rheinland; 2004.

[26] Standards Australia. AS4100 steel structures. Sydney (SA); 1998.

[27] Ranisch E-H. Zur Tragfähigkeit von Verklebungen zwischen Baustahl und Beton: geklebte Bewehrung: Inst. für Baustoffe, Massivbau und Brandschutz der Techn. Univ.: 1982.

[28] Brosens K, Van Gemert D. Plate end shear design for external CFRP laminates. Fracture mechanics of concrete structures. 3. AEDIFICATIO Publishers; 1998. 1793-804.

[29] Yuan H, Wu ZS, Yoshizawa H. Theoretical solutions on interfacial stress transfer of externally bonded steel/composite laminates. J Struct Mech Earthquake Eng 2001;675:27–39. Japan Society of Civil Engineers, Tokyo.

[30] Wu Z, Yuan H, Niu H. Stress transfer and fracture propagation in different kinds of adhesive joints. J Eng Mech 2002;128(5):562–73.

[31] Yuan H, Teng J, Seracino R, Wu Z, Yao J. Full-range behavior of FRP-to-concrete bonded joints. Eng Struct 2004;26(5):553–65.

[32] Nakaba K, Kanakubo T, Furuta T, Yoshizawa H. Bond behavior between fiber-reinforced polymer laminates and concrete. Struct J 2001;98(3):359–67.

[33] Wu Z, Yin J. Fracturing behaviors of FRP-strengthened concrete structures. Eng Fract Mech 2003;70(10):1339–55.

[34] Xia S, Teng J. Behaviour of FRP-to-steel bonded joints. Proceedings of the

international symposium on bond behaviour of FRP in structures: International Institute for FRP in Construction; 2005. p. 419–26.

[35] Fawzia S, Zhao X-L, Al-Mahaidi R. Bond–slip models for double strap joints strengthened by CFRP. Compos Struct 2010;92(9):2137–45.

[36] Yu T, Fernando D, Teng J, Zhao X. Experimental study on CFRP-to-steel bonded interfaces. Compos B Eng 2012;43(5):2279–89.

[37] Campilho R, De Moura M, Domingues J. Using a cohesive damage model to predict the tensile behaviour of CFRP single-strap repairs. Int J Solids Struct 2008;45(5):1497–512.

[38] Alfano G, Crisfield M. Finite element interface models for the delamination analysis of laminated composites: mechanical and computational issues. Int J Numer Meth Eng 2001;50(7):1701–36.

[39] Alfano G. On the influence of the shape of the interface law on the application of cohesive-zone models. Compos Sci Technol 2006;66(6):723–30.

[40] Campilho R, Banea MD, Pinto A, da Silva LF, de Jesus A. Strength prediction of single-and double-lap joints by standard and extended finite element modelling. Int J Adhes Adhes 2011;31(5):363–72.

[41] Qiu C, Feng P, Yang Y, Zhu L, Bai Y. Joint capacity of bonded sleeve connections for tubular fibre reinforced polymer members. Compos Struct 2017;163:267–79.

[42] Kato B, Mukai A. Bolted tension flanges joining square hollow section members. J Constr Steel Res 1985;5(3):163–77.

[43] Packer JA, Bruno L, Birkemoe PC. Limit analysis of bolted RHS flange plate joints. J Struct Eng 1989;115(9):2226–42.

[44] Willibald S, Packer J, Puthli R. Experimental study of bolted HSS flange-plate connections in axial tension. J Struct Eng 2002;128(3):328–36.

[45] AISC. Hollow structural sections connections manual. Chicago; 1997.

[46] EN 1993-1-8. Eurocode 3: design of steel structures, part 1–8: design of joints. Bryssels: CEN; 2005.

[47] Heinisuo M, Ronni H, Perttola H, Aalto A, Tiainen T. End and base plate joints with corner bolts for rectangular tubular member. J Constr Steel Res 2012;75:85–92.

[48] Wang Y, Zong L, Shi Y. Bending behavior and design model of bolted flange-plate connection. J Constr Steel Res 2013;84:1–16.

[49] Wheeler A, Clarke M, Hancock G. FE modeling of four-bolt, tubular moment end-plate connections. J Struct Eng 2000;126(7):816–22.

[50] Teng J, Fernando D, Yu T, Zhao X. Treatment of steel surfaces for effective adhesive bonding. Advances in FRP composites in civil engineering Springer; 2011. 865–8.

[51] Satasivam S, Bai Y, Yang Y, Zhu L, Zhao X-L. Mechanical performance of two-way modular FRP sandwich slabs. Composite Structures 2018;184:904–16.

[52] Xie L, Bai Y, Qi Y, Caprani C, Wang H. Compressive performance of PFRP SHS columns: effects of width-thickness ratio. Proceedings of the Institution of Civil Engineers/Structure and buildings. 2018; In-press.

[53] ASTM International. Standard Test Method for Tensile Properties of Polymer Matrix Composite Materials. ASTM D3039. West Conshohocken, PA. 2014.

[54] ASTM International. Standard Test Method for Short-Beam Strength of Polymer Matrix Composite Materials and Their Laminates. ASTM D2344. West Conshohocken, PA. 2016.

[55] Lee S, Munro M, Scott R. Evaluation of three in-plane shear test methods for advanced composite materials. Composites 1990;21(6):495–502.

[56] ASTM International. Standard Test Methods and Definitions for Mechanical Testing of Steel Products. ASTM A370–16. West Conshohocken, PA. 2016.

[57] ASTM International. Standard Test Method for Tensile Properties of Plastics. ASTM D638–10. West Conshohocken, PA. 2010.

[58] Trahair N, Bradford M. The Behaviour and Design of Steel Structures to AS 4100. Third Edition Taylor & Francis; 1998.

[59] Da Silva LF, Campilho RD. Advances in numerical modelling of adhesive joints. Advances in numerical modeling of adhesive joints Springer; 2012. 1–93.

[60] Lee MJ, Cho TM, Kim WS, Lee BC, Lee JJ. Determination of cohesive parameters for a mixed-mode cohesive zone model. Int J Adhes Adhes 2010;30(5):322–8.